Research Square

Preprints are preliminary reports that have not undergone peer review.
They should not be considered conclusive, used to inform clinical practice,
or referenced by the media as validated information.

Optimization of Post-processing Reconstruction for Orthopedic Metal Implants on Photon-Counting Detector CT: A Within-Patient Comparison

Mei Deng
Sun Yat-sen University Cancer Center
Jun Liu
Sun Yat-sen University Cancer Center
Haoqiang He
Sun Yat-sen University Cancer Center
Fengting Zhu
Sun Yat-sen University Cancer Center
Sisi Huang
Sun Yat-sen University Cancer Center
Li'an Luo
Siemens Healthineers Ltd
Lueqin Huang
Siemens Healthineers Ltd
Chuanmiao Xie
xchuanm@sysucc.org.cn

Sun Yat-sen University Cancer Center

Research Article

Keywords: photon-counting detector CT, orthopedic implants, metal artifact reduction, virtual monoenergetic imaging, image reconstruction

Posted Date: November 6th, 2026

DOI: https://doi.org/10.21203/rs.3.rs-11190317/v1

License: This work is licensed under a Creative Commons Attribution 4.0 International License.
Read Full License

Additional Declarations: No competing interests reported.

Abstract

Objectives

To determine how iterative metal artifact reduction (iMAR), virtual monoenergetic imaging (VMI), and reconstruction kernel selection affect metal artifacts and image quality around orthopedic implants on photon-counting detector CT (PCD-CT), and to identify task-specific reconstructions for bone and soft-tissue evaluation.

Materials and methods

This retrospective within-patient study included 10 patients with 11 orthopedic implant sites. All reconstructions were generated from the same PCD-CT raw data. Three predefined comparisons were performed: iMAR off versus on at 70 keV/Br40/1.0 mm; four bone reconstructions combining T3D or 145-keV VMI with Qr64 or Br64 at 0.4 mm; and four soft-tissue reconstructions combining T3D or 65-keV VMI with Br40 or Qr40 at 1.0 mm. CT attenuation, image noise, artifact index (AI), signal-to-noise ratio (SNR), contrast-to-noise ratio (CNR), 5-point Likert scores, and interreader agreement were evaluated.

Results

With matched parameters, iMAR increased median bone scores from 2 to 4 and soft-tissue scores from 1 to 2–3. For bone, 145-keV VMI reduced image noise and AI compared with T3D; 145-keV Br64 had the highest subjective scores, whereas 145-keV Qr64 showed the most favorable quantitative metrics. For soft tissue, T3D had lower noise and AI and higher SNR than 65-keV VMI, and T3D Br40 received the highest subjective scores. Weighted κ ranged from 0.635 to 0.717.

Conclusion

Post-processing optimization on PCD-CT was task specific. iMAR improved image evaluability, 145-keV VMI favored bone and bone-implant interface assessment, and T3D Br40 favored adjacent soft-tissue evaluation.

1 Introduction

CT is routinely used to evaluate patients after fracture fixation, spinal instrumentation, joint replacement, and implant reconstruction following bone tumor resection. Follow-up imaging must depict implant position and integrity, periprosthetic bone change, component loosening, and abnormalities in adjacent soft tissues [1–4]. Metal, however, can produce severe streaking and attenuation distortion that obscures both the interface and surrounding tissues, particularly in large porous titanium implants and multicomponent fixation systems [5–10].

CT metal-induced artifacts arise from several mechanisms, including photon starvation, scatter radiation, beam hardening, partial-volume effect, and inconsistent projection data [11, 12]. These artifacts can be mitigated by hardware- and software-based strategies: photon-counting-detector CT (PCD-CT) with direct-conversion detectors enables spectral imaging and high-resolution reconstruction, improving bone-implant-interface sharpness by 35–42% and bone-cement-interface sharpness by 28–43% relative to energy-integrating-detector CT (EID-CT) [13, 14]; metal-artifact-reduction algorithms (e.g., iterative metal-artifact-reduction, iMAR) correct metal-contaminated projection data to reduce severe streaks and abnormal CT-value shifts [15, 16]; spectral-derived virtual monoenergetic images (VMI) at high energy levels alleviate partial beam-hardening artifacts but may lower tissue contrast [17]. Reconstruction kernels modulate the balance among spatial resolution, image noise and texture. Sharper kernels facilitate visualization of the bone texture and implant margins yet may increase noise; smoother kernels improve image homogeneity but can reduce the sharpness at the bone-implant interface [13, 18, 19]. Therefore, different diagnostic tasks may require distinct parameter combinations: a setting that improves cortical and bone-implant interface sharpness may not provide the best depiction of adjacent soft tissues.

Previous PCD-CT studies have largely evaluated selected VMI levels, iMAR, or limited reconstruction settings in specific implants or anatomic regions [18, 20–23]. For clinical cases of large postoperative implants in bone-tumor patients requiring simultaneous evaluation of both bone and soft-tissue components, the relative effects of different post-processing parameters on identical raw data remain to be clarified. This study focuses on post-processing reconstruction. An intra-patient comparison was performed to investigate the effects of iMAR activation status, image type, VMI energy level, and reconstruction kernel on metal artifacts and image quality, with the aim of identifying task-specific post-processing strategies for bone and soft-tissue evaluation.

2 Materials and methods

2.1 Study design and ethics

This single-center retrospective exploration study was a secondary analysis of a prospectively acquired dataset and used a within-patient repeated-measures design. The original prospective study was approved by the Ethics Committee of Sun Yat-sen University Cancer Center (No. C2025-006-01), and all participants provided written informed consent that permitted secondary image post-processing analyses. The study was conducted in accordance with the Declaration of Helsinki and reported according to STROBE [24]. All CT examinations were clinically indicated; no additional acquisition, scan-range extension, or radiation exposure was introduced for this analysis.

2.2 Participants

Consecutive adults who underwent PCD-CT and had an orthopedic metal implant were screened from March 4 to April 16, 2026. Inclusion criteria were age 18 years or older, complete coverage of the implant and adjacent tissues, raw spectral data sufficient for all predefined reconstructions, matched image

plane/field of view/matrix across reconstructions, and no severe motion artifact affecting measurement. Exclusion criteria were missing raw data, incomplete implant coverage, inability to define a distal or contralateral reference region of interest (ROI), or substantial external metal or other inseparable artifacts. Ten patients with 11 implant sites were included; one patient contributed both thoracic and lumbar spinal sites. The implant site was the unit of analysis.

2.3 PCD-CT acquisition and reconstruction

All examinations were acquired with a NAEOTOM Alpha.Prime PCD-CT system (Siemens Healthineers), and post-processing was performed with syngo.via VC10. Acquisition parameters included 140 kV with automatic tube-current modulation, 120 × 0.2-mm detector collimation, Quantum HD mode, pitch 0.85, and 0.5-second rotation time. Bone reconstructions used a 1024 × 1024 matrix and soft-tissue reconstructions a 512 × 512 matrix. Slice thickness/increment was 1.0/0.7 mm or 0.4/0.2 mm according to the predefined task. When iMAR was enabled, the HIP preset was used. Quantum iterative reconstruction (QIR) was fixed at level 3 for all study reconstructions and was not evaluated as an independent variable.

2.4 Post-processing comparison framework

All images were reconstructed from the same raw dataset. To avoid simultaneous changes in image type, VMI energy, kernel, and slice thickness, three predefined comparison modules were used (Table 1). Module A compared iMAR off and on with 70-keV VMI, Br40, and 1.0-mm thickness held constant. Module B evaluated bone using four combinations of T3D or 145-keV VMI with Qr64 or Br64, with iMAR enabled and thickness fixed at 0.4 mm. Module C evaluated soft tissue using four combinations of T3D or 65-keV VMI with Br40 or Qr40, with iMAR enabled and thickness fixed at 1.0 mm. Slice thickness was task specific and was not analyzed as an independent factor.

Table 1
Post-processing reconstruction comparison framework.

Module	Research question	Fixed parameters	Parameters compared	Reconstruction settings
A: iMAR on/off	Does iMAR improve the subjective evaluability of images containing metal implants?	70 keV, Br40, 1.0 mm	iMAR disabled vs enabled	A1 non-iMAR-70 keV-Br40-1.0 mm; A2 iMAR-70 keV-Br40-1.0 mm
B: Bone post-processing	Effects of image type and reconstruction kernel on periprosthetic bone artifacts and the bone-implant interface	iMAR enabled, 0.4 mm	Image type: T3D vs 145 keV VMI; Kernel: Qr64 vs Br64	B1 iMAR-T3D-Qr64-0.4 mm; B2 iMAR-145 keV-Qr64-0.4 mm; B3 iMAR-T3D-Br64-0.4 mm; B4 iMAR-145 keV-Br64-0.4 mm
C: Soft tissue post-processing	Effects of image type and reconstruction kernel on adjacent soft tissues	iMAR enabled, 1.0 mm	Image type: T3D vs 65 keV VMI; Kernel: Br40 vs Qr40	S1 iMAR-T3D-Br40-1.0 mm; S2 iMAR-65 keV-Br40-1.0 mm; S3 iMAR-T3D-Qr40-1.0 mm; S4 iMAR-65 keV-Qr40-1.0 mm

Notes: T3D denotes the conventional polyenergetic image exported from the scanner workstation; the manufacturer designation is retained. Br denotes Body Regular and Qr Quantitative Regular. The numbers 40 and 64 indicate kernel sharpness; higher values generally provide greater edge sharpness and spatial resolution at the cost of higher image noise.

2.5 Quantitative image analysis

This study took metal-artifact reduction and the evaluability of peri-implant structures as the primary evaluation outcomes. Quantitative metrics were CT attenuation, image noise (SD), artifact index (AI), signal-to-noise ratio (SNR), and contrast-to-noise ratio (CNR). A musculoskeletal radiologist with 5 years of experience placed ROIs on a reference reconstruction and copied the coordinates to corresponding reconstructions. ROIs were approximately 150 mm², and measurements from three adjacent sections were averaged. Sampling included periprosthetic bone, periprosthetic muscle, distal or contralateral reference tissue and fat. ROIs avoided the implant itself, cortical margins, vessels, and focal lesions.

AI was calculated as $\sqrt{\max(SD_{artifact}^2 - SD_{reference}^2, 0)}$. For bone analysis, SD in fat remote from the artifact served as the reference; for soft-tissue analysis, contralateral normal muscle was used. AI was therefore compared only within the same module. SNR was calculated as $|HU_{target}|/SD_{target}$. Bone

CNR used periprosthetic bone as the target and fat as background; soft-tissue CNR used periprosthetic muscle as the target and fat as background, with CNR calculated as |HU_target − HU_background|/SD_background.

2.6 Qualitative image analysis

Two musculoskeletal radiologists with 7 and 10 years of experience independently performed qualitative assessment. Readers were blinded to participant identity and reconstruction parameters, image order was randomized, and evaluations were performed on the same display system under standardized viewing conditions. Bone assessment included implant margin sharpness, metal artifact suppression, periprosthetic bone visualization, and bone-implant interface visualization. Soft-tissue assessment included soft-tissue contrast, muscle-fat boundary delineation, artifact interference, and diagnostic confidence. Each item was graded on a 5-point Likert scale, with higher scores indicating better image quality or less artifact (Table S1).

2.7 Statistical analysis

Statistical analysis was performed with SPSS Statistics version 29.0.0 (IBM). The implant site was the analysis unit (n = 11), and reconstructions from the same site were treated as repeated measurements. Quantitative variables are reported as mean ± SD and ordinal scores as median and interquartile range. In module A, the eight qualitative scores were compared between matched iMAR-off and iMAR-on images using paired Wilcoxon signed-rank tests. In modules B and C, quantitative metrics were compared using repeated-measures analysis of variance and qualitative scores using the Friedman test. Because this was an exploratory small-sample study, no post hoc pairwise testing was performed in modules B or C; between-reconstruction differences were interpreted descriptively. Interreader agreement was assessed with linear weighted Cohen κ. Two-sided $p < 0.05$ indicated statistical significance.

2.8 Selection of task-specific reconstructions

No reconstruction was defined as optimal from a single metric alone. For bone, priority was given to artifact behavior and AI, followed by implant margin and bone-implant interface visualization. For soft tissue, image noise, SNR, CNR, and artifact interference were considered first, followed by soft-tissue boundary definition and diagnostic confidence. When quantitative noise performance and subjective sharpness favored different reconstructions, both advantages were retained in the task-specific interpretation.

3 Results

3.1 Participant and implant characteristics

Ten patients contributed 11 implant sites: right radius (n = 2), right humerus (n = 1), thoracic spine (n = 1), lumbar spine (n = 1), calcaneus (n = 1), right shoulder (n = 2), pelvis (n = 2), and femur (n = 1). The median

volume CT dose index was 11.2 mGy (range, 5.33–18.2 mGy), and the median dose-length product was 396 mGy·cm (range, 117–1396 mGy·cm) (Table S2). Baseline characteristics are summarized in Table 2.

Table 2
Baseline characteristics of patients with orthopedic metal implants undergoing PCD-CT

Characteristic	Value
Number of patients	10
Number of implantation sites	11
Demographic characteristics	
Age (years), mean ± SD	34.8 ± 9.8
Sex, male/female, n (%)	7 (70.0) / 3 (30.0)
Anatomic and surgery-related characteristics	
Actual examination date range of included cases	March 4 to April 16, 2026
Distribution of implantation sites, n (%)	
Upper extremity	5 (45.5)
Right radius	2 (18.2)
Right humerus	1 (9.1)
Right shoulder joint	2 (18.2)
Spine	2 (18.2)
Lumbar spine	1 (9.1)
Thoracic spine	1 (9.1)
Lower extremity/pelvic region	4 (36.4)
Calcaneus	1 (9.1)
Pelvis	2 (18.2)
Femoral head	1 (9.1)
Postoperative interval, by implantation site, n (%)	
< 6 months	1 (9.1)
6 months-2 years	3 (27.3)
> 2 years	7 (63.6)
Fixation method, by implantation site, n (%)	
Bone cement fixation	1 (9.1)

Note: Age and sex use the patient as the denominator (n = 10); implant location, postoperative interval, and fixation method use the implant site as the denominator (n = 11).

Characteristic	Value
Bone cement plus screw fixation	4 (36.4)
Screw fixation alone	3 (27.3)
Artificial vertebral body plus screw fixation	2 (18.2)
Implant plus screw fixation	1 (9.1)
Note: Age and sex use the patient as the denominator (n = 10); implant location, postoperative interval, and fixation method use the implant site as the denominator (n = 11).	

3.2 Effect of iMAR under matched parameters

At matched 70-keV/Br40/1.0-mm settings, enabling iMAR increased the median scores for implant margin sharpness, metal artifact suppression, periprosthetic bone visualization, and bone-implant interface visualization from 2 to 4. Median scores for soft-tissue contrast, muscle-fat boundary delineation, artifact interference, and diagnostic confidence increased from 1 to 2–3. The results support the use of iMAR as a baseline candidate artifact-reduction step under the parameter combinations applied in this study (Fig. 1).

3.3 Bone image quality

Quantitative bone results are shown in Table 3. Overall differences among the four bone reconstructions were significant for CT attenuation, SD, SNR, CNR, and AI (all $p < 0.05$). With Qr64, 145-keV VMI reduced SD from 196.00 ± 106.17 HU to 103.46 ± 56.41 HU and AI from 168.42 ± 118.48 to 81.18 ± 57.09 compared with T3D. With Br64, SD decreased from 255.55 ± 151.01 HU to 134.82 ± 67.54 HU and AI from 228.67 ± 165.65 to 100.97 ± 75.98. CT attenuation also decreased at 145 keV, whereas SNR was numerically higher and CNR changed little within the same kernel. Because CT attenuation is energy dependent and varies with tissue composition, it was not used alone to define artifact improvement.

Table 3
Quantitative image-quality metrics across reconstructions with iMAR enabled

Reconstruction setting	CT attenuation (HU)	SD (HU)	SNR	CNR	AI
Periprosthetic bone					
T3D-Qr64	297.27 ± 184.33	196.00 ± 106.17	1.61 ± 0.88	2.31 ± 3.61	168.42 ± 118.48
145 keV-Qr64	174.36 ± 117.27	103.46 ± 56.41	2.08 ± 1.58	2.40 ± 3.16	81.18 ± 57.09
T3D-Br64	292.91 ± 183.90	255.55 ± 151.01	1.23 ± 0.72	1.83 ± 2.85	228.67 ± 165.65
145 keV-Br64	165.36 ± 110.17	134.82 ± 67.54	1.39 ± 0.96	1.82 ± 2.29	100.97 ± 75.98
Periprosthetic soft tissue					
T3D-Br40	66.64 ± 50.81	20.09 ± 5.84	3.53 ± 2.56	11.84 ± 4.34	14.98 ± 4.62
65 keV-Br40	64.09 ± 79.48	32.27 ± 27.69	1.72 ± 1.56	12.16 ± 6.64	26.89 ± 29.47
T3D-Qr40	65.91 ± 50.51	19.36 ± 5.52	3.60 ± 2.62	12.54 ± 4.41	15.00 ± 4.71
65 keV-Qr40	64.09 ± 78.37	30.18 ± 24.45	1.84 ± 1.54	13.02 ± 6.49	25.61 ± 25.83

Qualitative bone results are summarized in Table 4 and Fig. 2. Overall differences among reconstructions were significant for implant margin sharpness, metal artifact suppression, periprosthetic bone visualization, and bone-implant interface visualization (all $p < 0.05$). The 145-keV Br64 reconstruction had median scores of 5 (IQR, 5–5), 5 (IQR, 4–5), 4 (IQR, 4–5), and 5 (IQR, 4–5), respectively, which were the highest among all groups; the corresponding scores for 145-keV Qr64 were 4 (IQR, 4–4), 4 (IQR, 4–4), 4 (IQR, 3–4), and 4 (IQR, 3–4).

Thus, 145-keV VMI consistently reduced bone image noise and AI relative to T3D at the same kernel. Kernel selection showed a trade-off: 145-keV Br64 provided the highest subjective scores for implant margins and the bone-implant interface, whereas 145-keV Qr64 provided lower SD and AI and a higher CNR (Fig. 3).

Table 4
Qualitative image-quality scores across reconstructions

Reconstruction setting	Implant margin sharpness	Metal artifact suppression	Periprosthetic bone visualization	Bone-implant interface visualization
non-iMAR-70 keV-Br40-1.0 mm	2 (2–2)	2 (2–2)	2 (2–2)	2 (2–2)
iMAR-70 keV-Br40-1.0 mm	4 (4–4)	4 (4–4)	4 (4–4)	4 (4–4)
iMAR-T3D-Qr64-0.4 mm	2 (2–3)	3 (2–3)	3 (2–3)	3 (2–3)
iMAR-145 keV-Qr64-0.4 mm	4 (4–4)	4 (4–4)	4 (3–4)	4 (3–4)
iMAR-T3D-Br64-0.4 mm	3 (3–3)	3 (3–3)	3 (3–3)	3 (3–3)
iMAR-145 keV-Br64-0.4 mm	5 (5–5)	5 (4–5)	4 (4–5)	5 (4–5)
Reconstruction setting	**Soft tissue contrast**	**Muscle-fat boundary delineation**	**Artifact interference with soft tissues**	**Diagnostic confidence**
non-iMAR-70 keV-Br40-1.0 mm	1 (1–2)	1 (1–2)	1 (1–1)	1 (1–1)
iMAR-70 keV-Br40-1.0 mm	3 (2–3)	2 (2–3)	2 (2–3)	2 (2–3)
iMAR-T3D-Br40-1.0 mm	3 (3–4)	3 (3–4)	3 (3–4)	3 (3–4)
iMAR-65 keV-Br40-1.0 mm	3 (2–3)	2 (2–3)	2 (2–2)	2 (2–3)
iMAR-T3D-Qr40-1.0 mm	2 (2–3)	3 (2–3)	3 (2–3)	2 (2–3)
iMAR-65 keV-Qr40-1.0 mm	3 (2–3)	2 (2–3)	2 (2–2)	2 (2–3)

3.4 Soft-tissue image quality

Quantitative soft-tissue results are shown in Table 3. Overall differences among T3D-Br40, 65-keV Br40, T3D-Qr40, and 65-keV Qr40 were significant for CT attenuation, SD, SNR, CNR, and AI (all $p < 0.05$).

At the same kernel, T3D showed lower image noise and AI and higher SNR than 65-keV VMI. With Br40, SD, AI, and SNR were 20.09 ± 5.84 HU, 14.98 ± 4.62, and 3.53 ± 2.56 for T3D versus 32.27 ± 27.69 HU, 26.89 ± 29.47, and 1.72 ± 1.56 for 65-keV VMI. With Qr40, the corresponding values were 19.36 ± 5.52 HU, 15.00 ± 4.71, and 3.60 ± 2.62 for T3D versus 30.18 ± 24.45 HU, 25.61 ± 25.83, and 1.84 ± 1.54 for 65-

keV VMI. CNR was numerically slightly higher at 65 keV (Br40, 12.16 ± 6.64 vs 11.84 ± 4.34; Qr40, 13.02 ± 6.49 vs 12.54 ± 4.41), whereas CT attenuation was similar.

Qualitative soft-tissue results are summarized in Table 4 and Fig. 2. Overall differences were significant for soft-tissue contrast, muscle-fat boundary delineation, artifact interference, and diagnostic confidence (all $p < 0.05$). T3D-Br40 had a median score of 3 (IQR, 3–4) for all four dimensions. T3D-Qr40 had median scores of 3 for muscle-fat boundary delineation and artifact interference and 2 for soft-tissue contrast and diagnostic confidence. Most scores for the two 65-keV VMI reconstructions were 2–3.

Overall, T3D provided lower noise and AI and higher SNR than 65-keV VMI for soft-tissue evaluation. T3D-Br40 had the highest descriptive scores across soft-tissue contrast, muscle-fat boundary delineation, artifact interference, and diagnostic confidence (Fig. 4).

3.5 Interreader agreement

Weighted κ values for interreader agreement ranged from 0.635 to 0.717 (95% CI, 0.496–0.856; all $p < 0.05$), indicating moderate-to-good agreement. Agreement was highest for metal artifact assessment ($\kappa = 0.717$; 95% CI, 0.608–0.827).

3.6 Task-specific reconstruction strategies

Task-specific reconstruction strategies derived from the quantitative and qualitative findings are summarized in Table 5. Representative bone and soft-tissue appearances are shown in Fig. 5.

Table 5
Task-specific post-processing strategies derived from study findings

Clinical task	Use	Setting	Key parameters	Main rationale	Typical application
Baseline configuration	Baseline	iMAR on + task-specific settings	iMAR on QIR level 3	Matched iMAR-on images had higher qualitative scores than iMAR-off images, supporting iMAR as the baseline artifact-reduction step.	All orthopedic metal implant PCD CT reconstructions
Bone assessment Goal: artifact reduction and bone-implant interface	Morph.	iMAR-145 keV-Br64-0.4 mm	iMAR on 145-keV VMI Br64 0.4 mm 1024 × 1024	Highest descriptive subjective scores; 145-keV VMI also reduced attenuation, noise, and AI versus T3D at the same kernel.	Osseointegration, suspected loosening, bone-implant interface, implant/bone-cement morphology
	Quant.	iMAR-145 keV-Qr64-0.4 mm	iMAR on 145-keV VMI Qr64 0.4 mm 1024 × 1024	Most favorable quantitative profile among tested bone reconstructions, with lower SD and AI and higher SNR/CNR.	Periprosthetic attenuation, artifact quantification, bone-density-related analysis
Soft-tissue assessment Goal: noise/artifact reduction and soft-tissue depiction	Routine	iMAR-T3D-Br40-1.0 mm	iMAR on T3D Br40 1.0 mm 512 × 512	Highest descriptive soft-tissue scores; lower SD and AI and higher SNR than 65-keV VMI.	Soft-tissue swelling, muscle injury, masses, routine postoperative follow-up
	Quant.	iMAR-T3D-Qr40-1.0 mm	iMAR on T3D Qr40 1.0 mm 512 × 512	Slightly lower SD and AI and higher SNR than Br40, with somewhat lower contrast and diagnostic-confidence scores.	Muscle attenuation, soft-tissue noise, and CNR measurement

4 Discussion

This within-patient study evaluated how iMAR, VMI energy, and reconstruction kernels affect image quality around orthopedic metal implants on PCD-CT. Three findings were central. First, with energy, kernel, and slice thickness matched, iMAR improved all eight qualitative image-quality scores. Second, for bone evaluation, 145-keV VMI reduced image noise and artifact burden relative to T3D, whereas kernel selection reflected a trade-off between subjective sharpness and quantitative stability: Br64 yielded the highest subjective scores and Qr64 the most favorable quantitative metrics. Third, for adjacent soft tissue, T3D showed lower noise and AI and higher SNR than 65-keV VMI, with T3D-Br40 receiving the highest descriptive subjective scores. Under the optimally-recommended image reconstruction protocol, satisfactory fine-detail visualization was achieved for different types of complex implants and the bone-implant interface (Fig. 6).

For the complex postoperative implants after bone tumor surgery, the present findings further support the value of PCD-CT as a high-resolution imaging platform for reducing metal artifacts and improving visualization of features relevant to osseointegration, osteolysis, and bone remodeling [25, 26]. The benefit of iMAR observed in this study is consistent with previous reports showing improved evaluation of metal-bone interfaces after correction of metal-corrupted projection data [12, 15, 17, 20, 23].

The bone findings also support the use of high-energy VMI in combination with iMAR for reducing artifacts around orthopedic implants, in agreement with previous studies [12, 27, 28]. Earlier work has shown that high-energy VMI in the range of approximately 110–150 keV can weaken beam-hardening effects and improve visualization of the bone-implant interface [17, 23]. In the present study, this advantage extended beyond relatively localized implants, such as dental hardware and spinal screws, to large and structurally complex postoperative implants after bone tumor surgery. At a fixed reconstruction kernel, 145-keV VMI reduced the AI of periprosthetic bone by more than 50% compared with T3D. In addition, the study demonstrated an important trade-off related to kernel selection under high-energy VMI with iMAR. Br64, a sharper Body Regular kernel, achieved the highest subjective visual scores and provided the clearest depiction of implant margins and the bone-implant interface, making it more suitable for routine morphologic interpretation. In contrast, the Qr64 Quantitative Regular kernel provided lower image noise, more stable CT attenuation, and better quantitative contrast performance, making it more suitable for objective applications such as quantitative CT analysis, radiomics, and bone-density-related measurements. Because previous metal artifact studies have focused mainly on energy level and artifact-reduction algorithms, the present findings add practical information regarding how reconstruction-kernel selection can be tailored to different clinical and quantitative tasks [13, 29].

Soft-tissue behavior differed markedly from the pattern observed for bone. In the present study, 65-keV low-energy VMI did not demonstrate the expected contrast advantage for peri-implant soft tissues and instead showed higher image noise and AI together with lower subjective image-quality scores than T3D. This finding contrasts with conventional spectral applications in abdominal imaging, where low-energy VMI can increase soft-tissue contrast by amplifying differences in x-ray attenuation and is commonly

used to improve lesion conspicuity in organs such as the liver and pancreas [30–32]. In the immediate vicinity of metal, however, low-energy photons are more readily absorbed by the implant, which may aggravate photon starvation and secondary beam-hardening effects. The resulting increase in image noise and artifact burden can therefore offset the theoretical gain in soft-tissue contrast. Similar observations have been reported in settings involving dental implants and implanted thoracic devices, suggesting that the usual strategy of using lower energy simply to increase contrast may not be directly applicable to soft tissues adjacent to metal [5, 20]. In our study, T3D combined with the Br40 kernel provided the most favorable overall balance among soft-tissue contrast, noise control, artifact suppression, and subjective diagnostic confidence. These results further emphasize the task-dependent nature of post-processing: reconstruction strategies should be matched to the specific anatomic target and diagnostic requirement rather than applied uniformly across all imaging tasks.

Clinical investigations of postoperative implants in bone-tumor patients and implant biomaterial research provide practical context and a feasible foundation for the evaluation metrics adopted in this study. Follow-up of porous titanium implants in the pelvis, femur, radius, and sacrum commonly requires assessment of radiolucent lines, osseointegration, periscrew bone loss, implant integrity, and tumor recurrence within adjacent soft tissues[4, 6–9]. Large solid implant components, porous surfaces, and multiple screws often render these imaging findings challenging to interpret. The present study did not test diagnostic accuracy for loosening, bone ingrowth, infection, or tumor recurrence; therefore, improved image quality should not be interpreted as evidence of enhanced lesion detection. Instead, these task-specific reconstruction strategies provide a reproducible framework for future diagnostic outcome studies.

This study had several limitations. First, it was a single-center exploratory analysis of 10 patients and 11 implant sites, with heterogeneity in anatomic location, implant type, and metal configuration. Second, all data were obtained from one PCD-CT platform; slice thickness was linked to the imaging task, QIR was fixed at level 3, and interactions among slice thickness, iterative reconstruction strength, kernel, and VMI energy were not independently evaluated. Third, without a conventional EID-CT comparator, this study was unable to directly quantify the diagnostic benefit of PCD-CT over conventional CT in orthopedic-implant imaging. Fourth, ROI measurements and qualitative scores may be influenced by anatomy, implant orientation, patient positioning, and reader experience. Fifth, iMAR can generate secondary low-attenuation bands or dark-edge artifacts around large or complex implants, which were not independently graded or quantified. Finally, the study evaluated image quality rather than diagnostic accuracy, and the proposed reconstructions require validation in larger multicenter cohorts.

5 Conclusions

In orthopedic metal implant imaging with PCD-CT, post-processing performance was task dependent. iMAR improved image evaluability under matched conditions. For bone and bone-implant interface assessment, 145-keV VMI was favored, with Br64 better suited to morphologic interpretation and Qr64 to quantitative analysis. For adjacent soft tissue, T3D with Br40 provided the most balanced performance.

Larger studies are needed to determine whether these image-quality advantages improve diagnostic performance.

Abbreviations

Full term
AI
Artifact index
CNR
Contrast-to-noise ratio
EID-CT
Energy-integrating-detector computed tomography
iMAR
Iterative metal artifact reduction
PCD-CT
Photon-counting-detector computed tomography
QIR
Quantum iterative reconstruction
ROI
Region of interest
SNR
Signal-to-noise ratio
VMI
Virtual monoenergetic imaging

Declarations

Ethics approval and consent to participate

The study was approved by the Ethics Committee of Sun Yat-sen University Cancer Center (No. C2025-006-01). All participants provided written informed consent permitting secondary image post-processing analyses.

Consent for publication

All patients provided written informed consent for publication of anonymized image data.

Competing interests

Two of the authors, Lueqin Huang and Li'an Luo, are employees of Siemens Healthineers, but they were not involved in the analysis of the data and had no control of data or information submitted for publication. There are no conflict of interests or industry support for this study.

Funding

This work received no specific grant from any funding agency in the public, commercial, or not-for-profit sectors.

Author Contribution

MD and JL conceived and designed the study. HH and CX supervised the project, MD and JL collected image data. FZ ,SH and MD performed image evaluation,quantitative and qualitative analysis. LH and LL provided technical reconstruction consultation. MD drafted the manuscript. All authors contributed to manuscript revision,read and approved the final version of the manuscript.

Acknowledgement

The authors are grateful to radiologists Liangru Ke for participating in the reader study, and to radiographers Zhida Yu and Wei Luo for assistance in image acquisition. AI-based language-editing tools (ChatGPT) were used solely to improve grammar and language flow; no content was generated by AI.

Availability of data and materials

The datasets used and/or analysed during the current study are available from the corresponding author on reasonable request. Restrictions may apply due to licensing and/or regulatory reasons.

References

1. Foti G, Fighera A, Campacci A, Natali S, Guerriero M, Zorzi C, et al. Diagnostic Performance of Dual-Energy CT for Detecting Painful Hip Prosthesis Loosening. Radiology. 2021;300(3):641–9. 10.1148/radiol.2021203510.
2. Foti G, Longo C, D'Onofrio M, Natali S, Piovan G, Oliboni E, et al. Dual-Energy CT for Detecting Painful Knee Prosthesis Loosening. Radiology. 2023;306(3):e211818. 10.1148/radiol.211818.
3. Shet SS, Kakish E, Murphy SC, Roopnarinesingh R, Power SP, Maher MM, et al. Imaging evaluation of periprosthetic loosening: A primer for the general radiologist. World J Radiol. 2025;17(2). 10.4329/wjr.v17.i2.102373.

4. Benady A, Yehiel N, Segal O, Merose O, Sterenheim A, Sher O, et al. Knee-Sparing Resection and Reconstruction Surgery for Bone Sarcoma Using 3D-Surgical Approach: Average of 5-Year Follow-Up. Medicina. 2025;61(3):476. 10.3390/medicina61030476.
5. Haag F, Hokamp NG, Overhoff D, Dasegowda G, Kuru M, Nörenberg D, et al. Potential of photon counting computed tomography derived spectral reconstructions to reduce beam-hardening artifacts in chest CT. Eur J Radiol. 2024;175:111448. 10.1016/j.ejrad.2024.111448.
6. Tan L, Li Y, Hu X, Wang Y, Zhang X, Liu X, et al. Clinical Application of 3D -Printed Custom Hemipelvic Prostheses With Re-Entrant Chiral Structure in Reconstruction After Pelvic Tumor Resection. Orthop Surg. 2025;17(11):3067–77. 10.1111/os.70159.
7. Cevolani L, Spazzoli B, Staals EL, Errani C, Campanacci L, Spinnato P, et al. 3D -Printed Cut Guides and Custom Prostheses for Pelvic Reconstruction in Bone Sarcoma Patients: Complications, Survival Rates, and Functional Outcomes. Orthop Surg. 2026;18(2):311–21. 10.1111/os.70192.
8. Shi Q, Zhu J, Liang H, Wang R, Huang S, Guo W, et al. How precise is excision and reconstruction using 3D printing technology for total sacrectomy: accuracy validation in 9 consecutive cases. 3D Print Med. 2025;11(1):42. 10.1186/s41205-025-00295-6.
9. Wang T, Ma X, Zhang Y, Li J, Han L, Nabil Z, ul H, et al. A retrospective study of 3D-printed custom titanium prostheses for reconstruction of bone defects after resection of pelvic tumors: technical points and early results. BMC Surg. 2025;25(1):513. 10.1186/s12893-025-03253-5.
10. Shao X, Dou M, Yang Q, Li J, Zhang A, Yao Y, et al. Reconstruction of massive bone defects after femoral tumor resection using two new-designed 3D-printed intercalary prostheses: a clinical analytic study with the cooperative utilization of multiple technologies. BMC Musculoskelet Disord. 2023;24(1):67. 10.1186/s12891-023-06171-w.
11. Barrett JF, Keat N. Artifacts in CT: Recognition and Avoidance. Radiographics. 2004;24(6):1679–91. 10.1148/rg.246045065.
12. Pallasch FB, Rau A, Reisert M, Rau S, Diallo T, Stein T, et al. Photon-counting detector computed tomography for metal artifact reduction: a comparative study of different artifact reduction techniques in patients with orthopedic implants. Radiol med. 2024;129(6):890–900. 10.1007/s11547-024-01822-x.
13. Woisetschläger M, Booij R, Tesselaar E, Oei EHG, Schilcher J. Improved visualization of the bone-implant interface and osseointegration in ex vivo acetabular cup implants using photon-counting detector CT. Eur Radiol Exp. 2023;7(1):19. 10.1186/s41747-023-00335-y.
14. Willemink MJ, Persson M, Pourmorteza A, Pelc NJ, Fleischmann D. Photon-counting CT: Technical Principles and Clinical Prospects. Radiology. 2018;289(2):293–312. 10.1148/radiol.2018172656.
15. Demmert TT, Schikorra T, Heining SM, Specovius A, Klambauer K, Moser LJ, et al. Advanced Iterative Metal Artifact Reduction With Intrinsic Spectral Information From Photon-counting Detector Computed Tomography: Improving the Assessment of Metal-bone Interface. Invest Radiol. 2026 Feb;25. 10.1097/RLI.0000000000001282.

16. Kara M, Shatat A, Dönmez MK, Tosun M, Uslu H, Yalnız A, et al. Effectiveness of single-energy metallic artifact reduction in CT angiography for patients with lower extremity metallic implants. Clin Radiol. 2026;93:107217. 10.1016/j.crad.2025.107217.
17. Marth T, Marth AA, Abel F, Paul Marcus R, Fritz B, Specovius A, et al. Metal Artifact Reduction in Lumbar Spine Instrumentation: A Comparison of Photon-Counting Detector–Computed Tomography Versus Energy-Integrating Detector–Computed Tomography, Iterative Metal Artifact Reduction, and Virtual Monoenergetic Imaging in 100 Examinations. Invest Radiol. 2026 Feb;16. 10.1097/RLI.0000000000001276.
18. Björkman AS, Malusek A, Persson A, Gauffin H, Koskinen SK. Photon-counting CT: image quality evaluation in patients with tibial plateau fracture treated with metallic osteosynthesis material. Eur Radiol Exp. 2026;10(1):96. 10.1186/s41747-026-00761-8.
19. Qin L, Zhou S, Dong H, Li J, Zhang R, Yang C, et al. Improvement of coronary stent visualization using ultra-high-resolution photon-counting detector CT. Eur Radiol. 2024;34(10):6568–77. 10.1007/s00330-024-10760-1.
20. Schreck J, Niehoff JH, Saeed S, Kroeger JR, Lennartz S, Laukamp KR, et al. Dental implant artifacts: Evaluation of photon counting CT-derived virtual monoenergetic images in combination with iterative metal artifact reduction algorithms. Eur J Radiol. 2025;187:112117. 10.1016/j.ejrad.2025.112117.
21. Thater G, Frerichs I, Büttner S, Schoenberg SO, Froelich M, Ayx I. Reduction of Streak Artifacts in the Superior Vena Cava for Better Visualization of Mediastinal Structures Through Virtual Monoenergetic Reconstructions Using a Photon-counting Detector Computed Tomography. J Thorac Imaging. 2025;40(4). 10.1097/RTI.0000000000000822.
22. Kämmerling N, Farnebo S, Sandstedt M, Booij R, Persson A, Tesselaar E. Assessment of metal artifacts from titanium wrist prostheses: photon-counting versus energy-integrating detector CT. Eur Radiol Exp. 2025;9(1):45. 10.1186/s41747-025-00587-w.
23. Abel F, Curti M, Marth T, Marcus RP, Farshad M, Sutter R. Photon-counting CT in Anterior Cervical Discectomy and Fusion: Improved Metal Artifact Reduction and Impact on Bone Fusion Assessment. Invest Radiol. 2026 Jun;2. 10.1097/RLI.0000000000001298.
24. Elm EV, Altman DG, Egger M, Pocock SJ, Gøtzsche PC, Vandenbroucke JP. Strengthening the reporting of observational studies in epidemiology (STROBE) statement: guidelines for reporting observational studies. BMJ. 2007;335(7624):806–8. 10.1136/bmj.39335.541782.AD.
25. Kämmerling N, Farnebo S, Lind G, Sandstedt M, Persson A, Tesselaar E. Evaluating osseointegration, bone remodeling and osteolysis after total wrist arthroplasty using photon-counting detector CT. Skeletal Radiol. 2026 Jun;3. 10.1007/s00256-026-05276-2.
26. Ma Y, Su D, Yang S, Miao Q, Bai Z, Li Y, et al. Photon-counting detector CT for bone defect repair: Unveiling the impact of pore size on osseointegration and the advantage over traditional imaging. Comput Biol Med. 2025;196:110881. 10.1016/j.compbiomed.2025.110881.

27. Popp D, Sinzinger AX, Decker JA, Braun F, Bette S, Risch F, et al. Spectral metal artifact reduction after posterior spinal fixation in photon-counting detector CT datasets. Eur J Radiol. 2023;165:110946. 10.1016/j.ejrad.2023.110946.
28. Marth AA, Goller SS, Kajdi GW, Marcus RP, Sutter R, Photon-Counting Detector CT. Clinical Utility of Virtual Monoenergetic Imaging Combined With Tin Prefiltration to Reduce Metal Artifacts in the Postoperative Ankle. Invest Radiol. 2024;59(8):545–53. 10.1097/RLI.0000000000001058.
29. Booij R, De Klerk P, Tesselaar E, Woisetschläger M, Brandts A, Olsthoorn M, et al. Assessment of bone-implant interface image quality for in-vivo acetabular cup implants using photon-counting detector CT: Impact of tin pre-filtration. Eur J Radiol Open. 2025;14:100646. 10.1016/j.ejro.2025.100646.
30. Huang R, Yang Y, Gao M, Xu Z, Dong H, Yan F, et al. Pancreatic imaging with ultra-high-resolution photon-counting computed tomography: Preliminary assessment of image quality. Eur J Radiol. 2026;195:112596. 10.1016/j.ejrad.2025.112596.
31. Alagic Z, Duran CV, Svensson-Marcial A, Koskinen SK. Contrast-enhanced photon-counting detector CT for discriminating local recurrence from postoperative changes after resection of pancreatic ductal adenocarcinoma. Eur Radiol Exp. 2025;9(1):26. 10.1186/s41747-025-00567-0.
32. Ichikawa S, Sofue K, Nakamura Y, Higaki T, Morisaka H, Hyodo T, et al. Single-Energy, Dual-Energy, and Photon-Counting Computed Tomography of the Liver: Current Development and Clinical Utility for the Assessment of Focal Liver Lesions. Invest Radiol. 2026;61(3):175–84. 10.1097/RLI.0000000000001187.

Figures

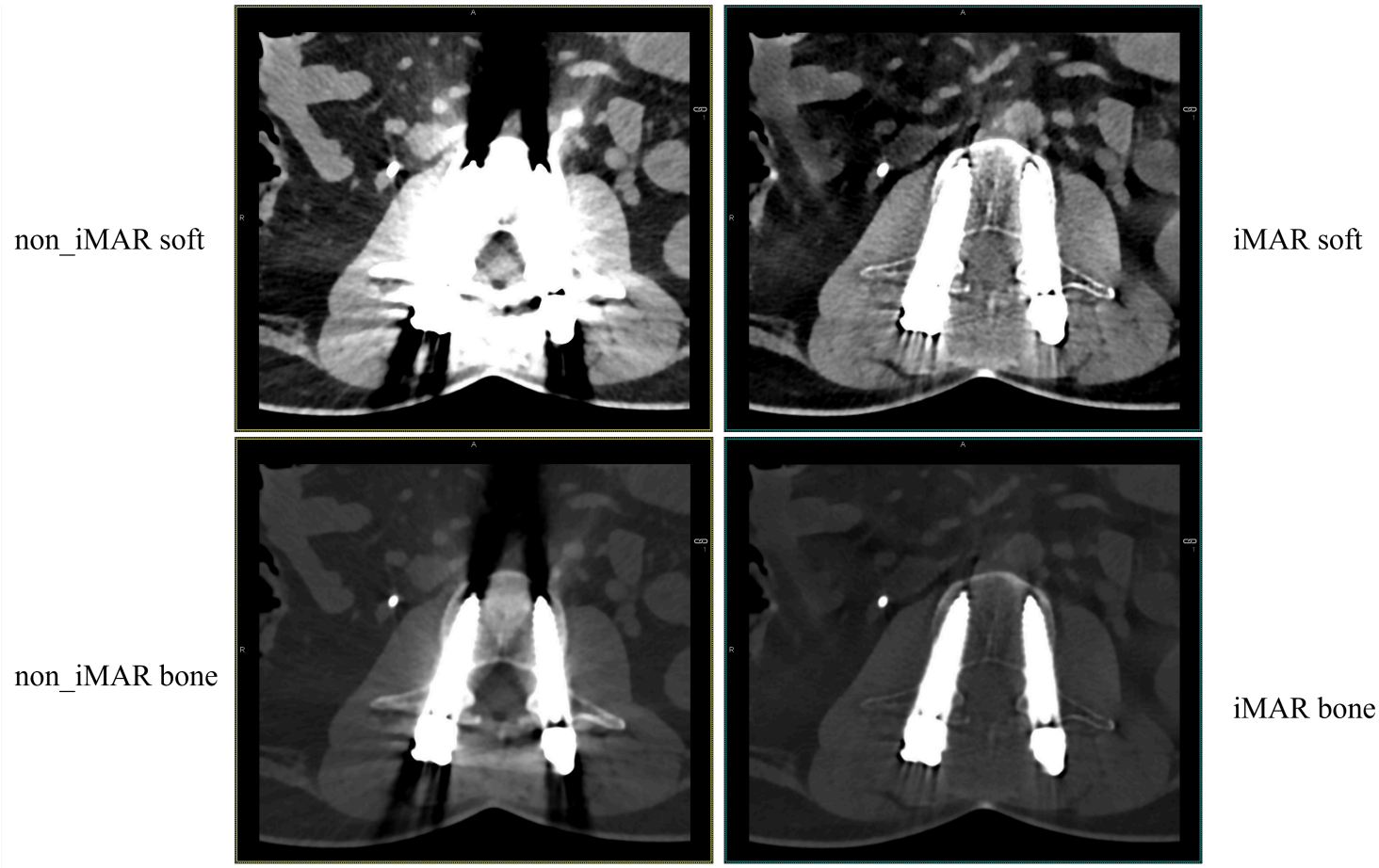


Figure 1

Lumbar fixation images reconstructed with iMAR off and on under matched 70-keV/Br40/1.0-mm conditions. Soft-tissue and bone windows are shown for both reconstructions.

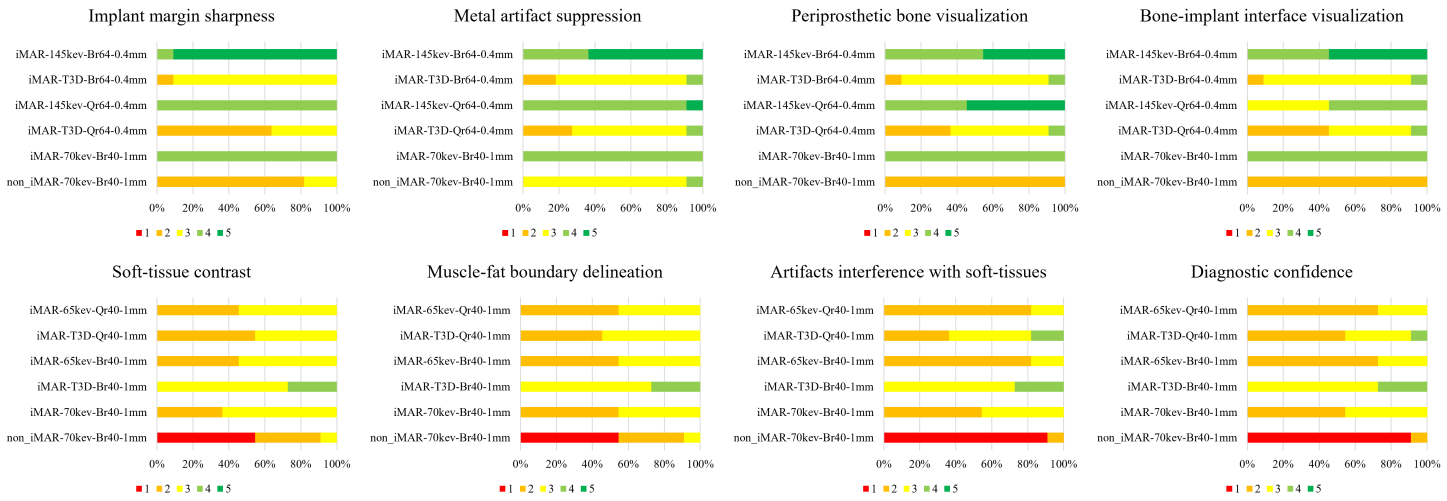


Figure 2

Distribution of qualitative image-quality scores across reconstruction settings.

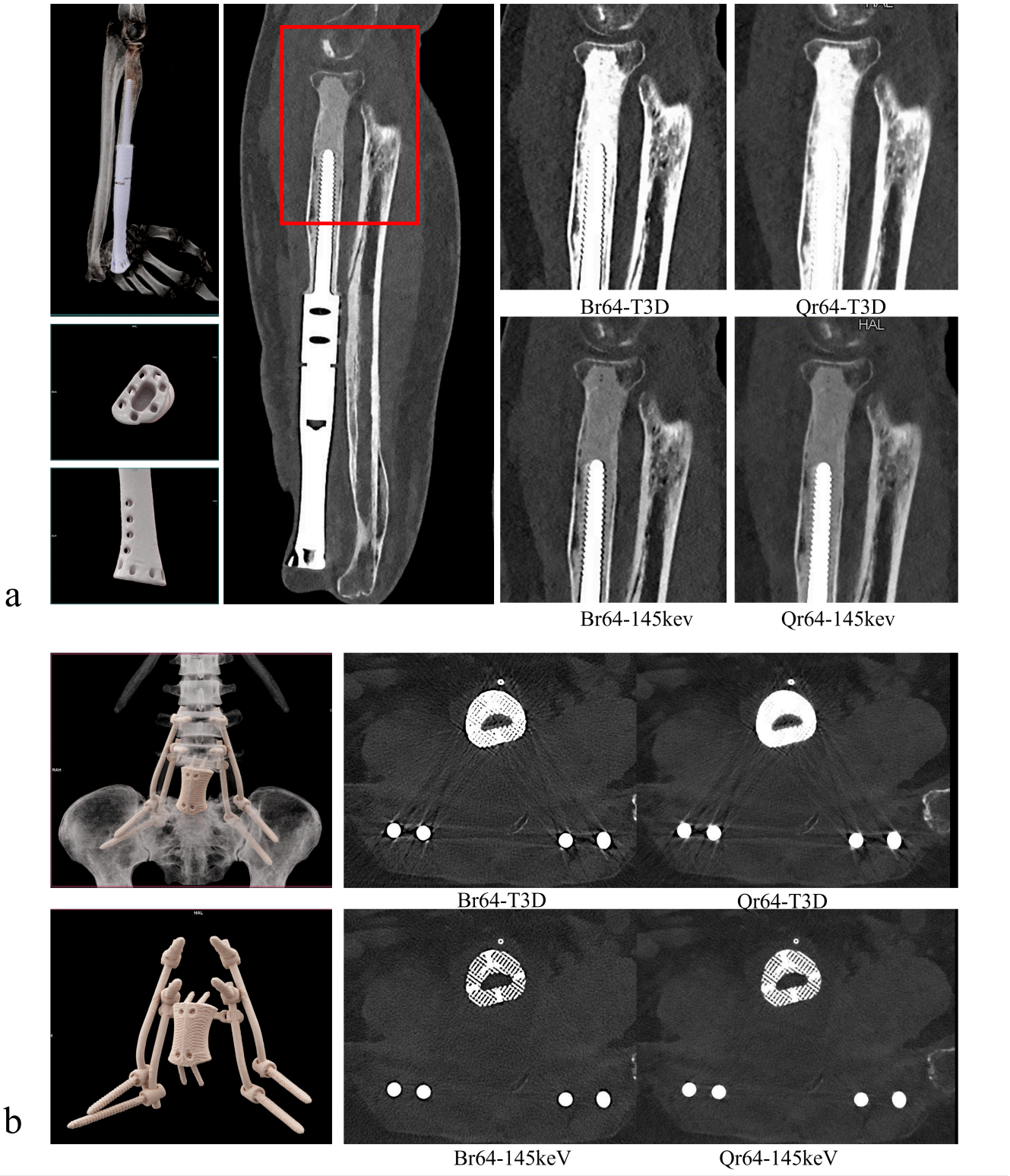


Figure 3

Bone reconstructions using T3D-Qr64, 145-keV Qr64, T3D-Br64, and 145-keV Br64. iMAR was enabled and slice thickness was fixed at 0.4 mm; image plane, magnification, window width, and window level were matched. (a) Representative long-bone implant case showing osseous structures, implant margins, and bone cement. (b) Representative lumbar implant case showing streak artifacts and the bone-implant interface across reconstructions.

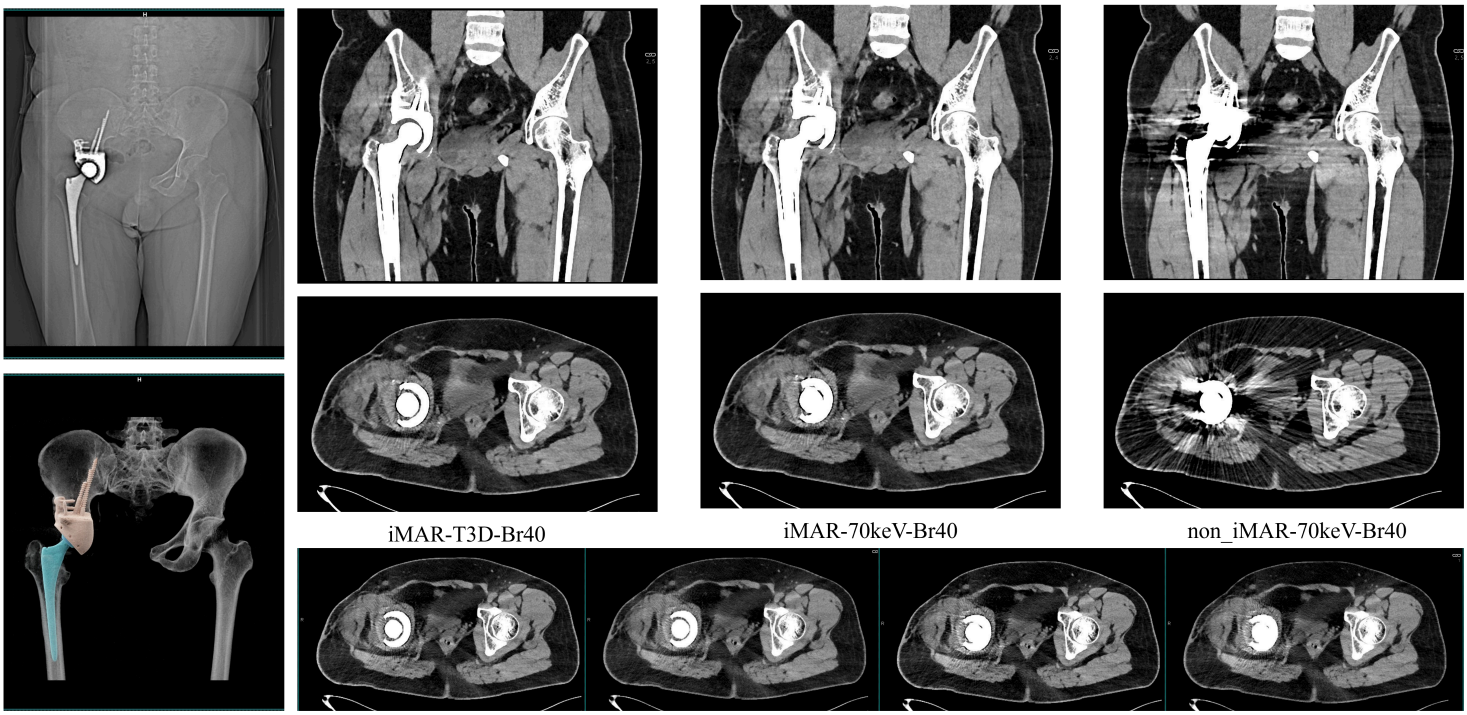


Figure 4

Hip implant images illustrating soft-tissue appearance across T3D, 65/70-keV VMI, and iMAR on/off settings.

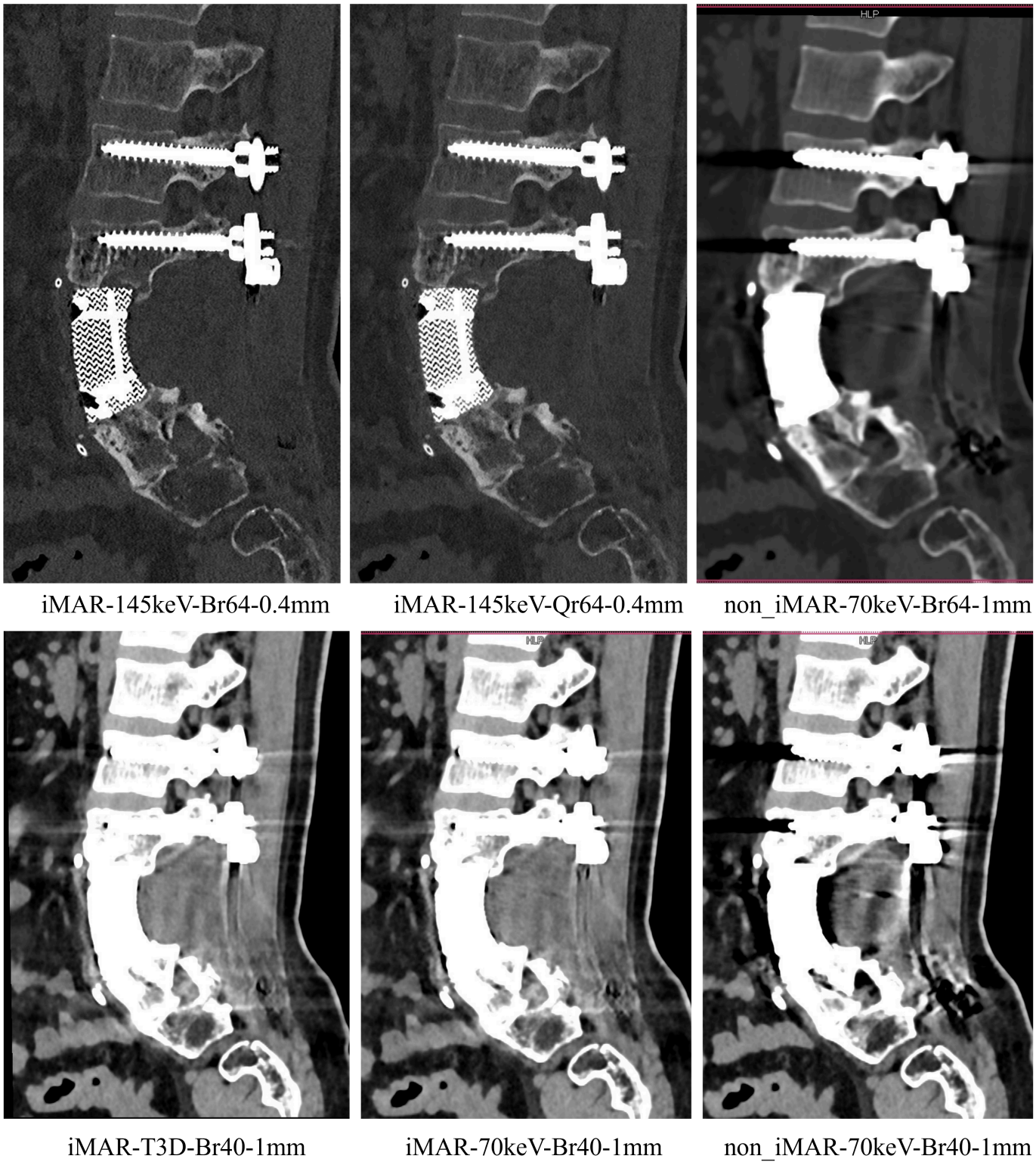


Figure 5

Lumbar implant images reconstructed with selected post-processing settings.

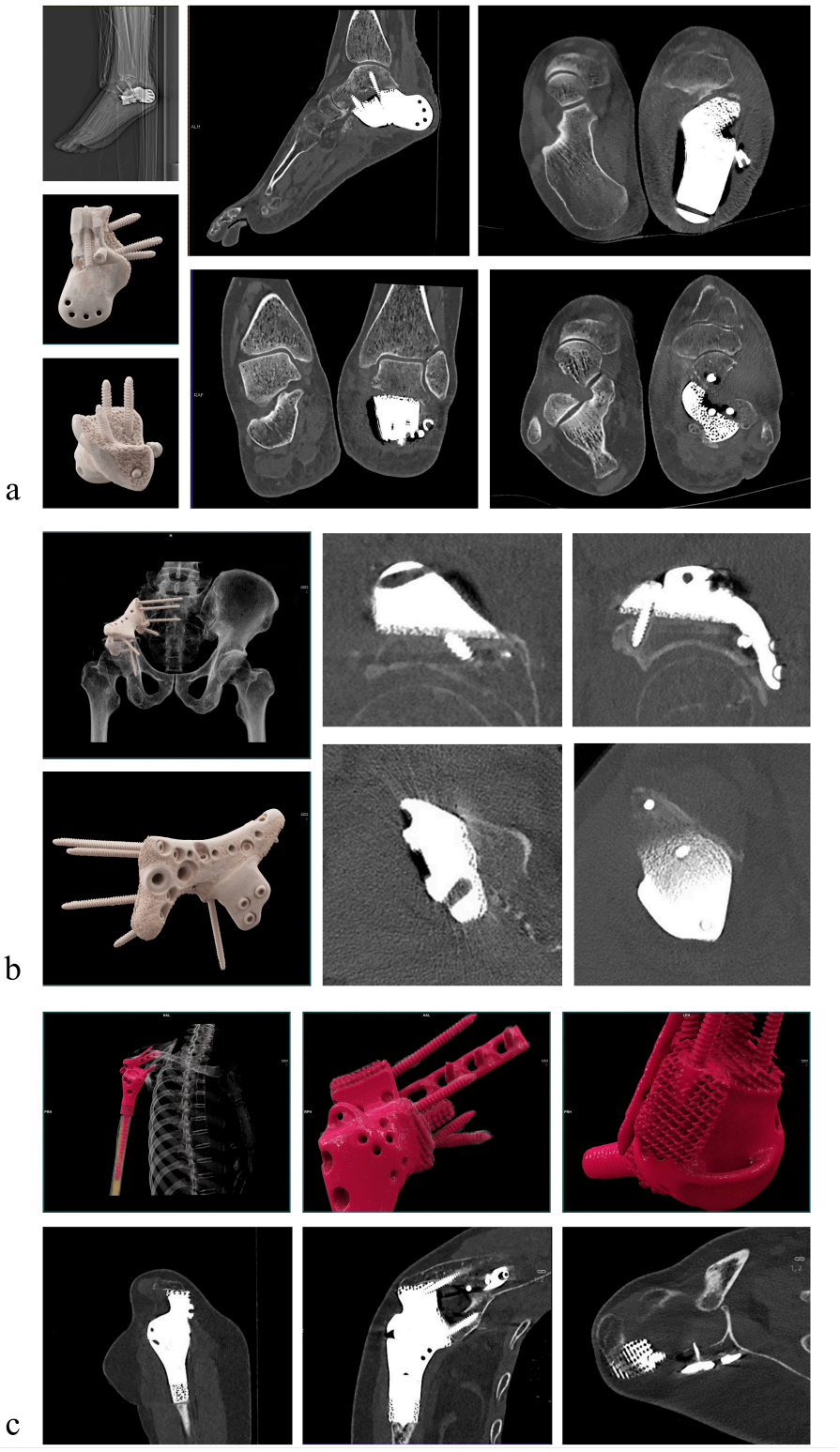


Figure 6

Complex implants of calcaneus (a), pelvis (b), and shoulder joint (c), revealing screw details, implant textures, and clear bone-implant marginal contact interfaces.

Supplementary Files

This is a list of supplementary files associated with this preprint. Click to download.

- SupplementaryTable1.docx
- SupplementaryTable2.docx